Modeling phase separation in solids beyond the classical nucleation theory: Application to FeCr

L. Luneville, O. Tissot, Cristelle Pareige, D. Simeone

Modeling phase separation in solids beyond the Classical Nucleation Theory: application to FeCr

L. Luneville,[1] O. Tissot,[1] C. Pareige,[2] and D. Simeone[1]

[1)] *Université Paris-Saclay, CEA, Service de Recherches en Matériaux et procédés Avancés, 91191, Gif-sur-Yvette, France*

[2)] *Univ. Rouen Normandie, INSA Rouen Normandie, CNRS, Groupe de Physique des Matériaux UMR 6634, F-76000 Rouen, France*

(*Electronic mail: laurence.luneville@cea.fr)

Despite a large amount of work was devoted to study the phase separation in solids, the underlying physical mechanism responsible for such diffusive first-order phase transitions remains difficult to model outside the spinodal regime, *i.e.* in the nucleation and growth regime. This work presents an alternative of the Classical Nucleation Theory, for modeling phase separation in this regime, even for systems far from the solubility limit, *i.e.* for high degree of meta-stability where the Classical Nucleation Theory does not hold. This method then allows a direct comparison between simulations and experiments always performed in solids with high degree of meta-stability.

I. INTRODUCTION

Diffusive first-order phase transitions in solids are largely widespread in nature and many works were devoted to model the microstructure resulting from this phase separation[1–4]. Such a transformation is very common in metallurgy and more generally in solid state physics[5,6]. Modeling microstructures resulting from solid-solid phase separation is crucial because it controls materials properties[6–8]. In contrast to second-order phase transitions, physical processes associated with diffusive first-order phase transitions cannot reduce to a simple mechanism[9]. Non-infinitesimal spatial fluctuations of composition must firstly be generated to initiate the phase transition overcoming an energy barrier associated with a metastable state[6,10,11]. This first process is known as the nucleation step. It leads to the appearance of stable spatial finite fluctuations of composition, known as critical precipitates in Classical Nucleation Theory (CNT). These critical precipitates then grow by depleting the matrix through diffusion. This growth process defines the second step of the phase separation. Finally, precipitates undergo Oswald ripening. This last mechanism favors the selection of large precipitates and defines the final complex microstructure controlling the materials' properties.

Modeling diffusive first-order phase transitions then requires a deep understanding of these three processes over a large range of meta-stability, *i.e.* whatever the value of the height of the energy barrier associated with the meta-stable state is. On the other hand, these three mechanisms may operate at the same time scale, right from the early stages, nucleation, growth and coarsening may be concomitant. A robust modeling of the interplay between these three mechanisms is still lacking.

The main reason for this lack stems from a number of difficulties: the formation of stable precipitates in a depleted matrix during the phase separation generates a long range order strain field able to modify not only the composition of precipitates but also their shape, blurring information on the underlying mechanisms responsible for the phase separation. Moreover, samples must be ultra-pure in order to avoid heterogeneous nucleation, energetically more favorable than homogeneous one, but highly dependent on impurities and defects (dislocations, grain boundary...) existing initially in the material. Models for studying the nucleation and growth have been largely developed within the theoretical framework of the Classical Nucleation Theory (CNT)[12]. However, this formalism is only valid near the solubility limit[13] where the experimental nucleation rate is very low. This point forbids performing any experimental measurements on a realistic time scale. Experimental microstructures resulting from the nucleation and growth process are thus only measured far from the solubility limit where the energy barrier computed from the CNT are no more realistic.

The aim of this article is to propose an alternative to the CNT for modeling solid-solid phase separation in the nucleation and growth regime.

Contrary to the CNT, our approach applies whatever the degree of meta-stability of the system is. It then becomes possible to validate our original model with a direct comparison between simulated and experimental microstructures extracted from Atom Probe Tomography (APT) measurements performed at different times. To reach this goal, different 3D microstructures resulting from the phase separation on ultra-pure *FeCr* samples were modeled in detail far from the solubility limit within the Phase Field formalism.

The phase separation in *FeCr* is a textbook example of diffusive first order phase transition. Our study focused on homogeneous phase separation in an ultra-pure *FeCr* alloy for several reasons:

- as Cr and Fe atoms possess similar atomic radii, the misfit in this alloy can then be neglected. The elastic energy resulting from the formation of Cr-rich precipitates is then negligible
- ultra-pure *FeCr* samples can be manufactured insuring that the nucleation is homogeneous during the nucleation step
- the α-α' phase separation in *FeCr* is iso-structural[14], *i.e.* space groups of high ($T > T_c = 1000K$) and low temperature phases ($T < T_c$) are identical. This implies that only one scalar order parameter, $c(\mathbf{x},t) - c_c$ is sufficient for describing the phase transition within the

Phase Field framework. Note that $c(\mathbf{x},t)$ is the local Cr atomic fraction and $c_c = \frac{1}{2}$ is the critical concentration at $T = T_c$.

To validate our approach, the evolution of the 3D microstructure for different $Fe_{1-\bar{c}}Cr_{\bar{c}}$ samples of Chromium mean composition $\bar{c}$ (in atomic fraction) has then been simulated and directly compared with results of APT measurements performed after isothermal annealing at $773K$. The choice of this annealing temperature is the best trade-off to observe phase separation at realistic times (2000 hours). Note that for this material and at this temperature, the nucleation and growth regime remains narrow, *i.e.* $\bar{c}$ varies from 0.14 to 0.23. However, the incubation time associated with the nucleation process is so large for $\bar{c} < 0.19$ that no phase separation can be observed over a realistic time scale at $T \leq 773K$. Moreover, for $\bar{c} > 0.22$, we are in the pseudo-spinodal regime in which the spinodal decomposition interferes with the nucleation and growth regime blurring the analysis of experimental results. Experiments and simulations have thus been performed varying $\bar{c}$ from 0.19 to 0.206. Even if this range seems to be narrow, it is sufficient to validate the approach proposed in this work.

In the first part of this work, the notion of stable precipitate in a finite volume is introduced for a conservative process. The second part of this paper is devoted to the Phase-Field (PF) modeling of the phase separation in the nucleation and growth regime. The third part of the paper highlights excellent agreement between 3D simulated and measured microstructures on ultra-pure *FeCr* samples annealed at $773K$. The last part of this works questions the validity of the Johnson[15], Mehl[16], Avrami[17] and Kolmogorov[18] theory (JMAK) extensively used to model the volume fraction of the new phase during a phase separation as a function of temperature and time in non conservative systems, such as for instance the grains growth[19].

II. STABLE PRECIPITATE IN FINITE VOLUME WITHIN THE PHASE-FIELD FORMALISM

Within the spinodal decomposition, the quenched high temperature system is unstable, *i.e.* it is a local maximum of the non-equilibrium free energy. Some infinitesimal thermal fluctuations may then amplify. Cahn and Hilliard[20–22] developed a diffusion-like equation, called the Cahn-Hilliard (CH) equation, to compute the evolution of such fluctuations within a Phase Field (PF) approach. The main interest of this equation is that the spatial distribution of precipitates and their growth rate are implicitly taken into account[5]. It then appears as an efficient tool for computing the evolution of the microstructure avoiding any modeling of interface motion between the Cr-rich precipitates and the Fe-rich matrix.

Within the nucleation and growth regime, the quenched high temperature phase is metastable, *i.e.* it is a local minimum of the non-equilibrium free energy. Extension of the CH equation to nucleation and growth regime suffers from a severe difficulty. Due to the existence of an energy barrier defined by the difference between the 1-index saddle point and the metastable non-equilibrium free energies, all infinitesimal thermal fluctuations vanish and the CH equation cannot strictly speaking be applied for modeling the nucleation and growth process. To overcome this difficulty, the CNT [23–25] was developed more than 100 years ago to compute the critical precipitate, the smallest non infinitesimal fluctuation able either to vanish or to amplify during the nucleation step. The key point of the CNT is to compute the characteristic size and the composition of critical precipitates. From its knowledge, not only the energy barrier but also the nucleation rate and the incubation time can be easily determined. Even if the CNT still today leads our current understanding of the phase separation phenomenon, it suffers from several drawbacks:

- the composition of critical precipitates are fixed to the solubility limits given by the equilibrium phase diagram at the temperature T. This prediction disagrees with experimental APT measurements performed on ultra-pure *FeCr* samples[26–28].
- the calculated energy barrier tends to a non null finite value approaching the spinodal line in disagreement with the null expected value.
- Unlike the phase-field technique, which generates precipitates by minimizing the concentration field $c(\mathbf{x},t)$ with time, Cr-rich precipitates have to be introduced "by hand" within the CNT. Their spatial distribution must then be intuited[29] within the CNT framework.

Within the PF formalism, nucleation is simulated adding a Langevin noise[5,30] to the CH equation. This provides an elegant treatment of nucleation overcoming limitations of the CNT. However, this approach is computationally expensive, since it requires sampling at a very high frequency the nucleation rate in order to observe nucleation events, which are very rare.

In this paper, we develop an hybrid model to adapt the PF approach for modeling the nucleation and growth steps. This is accomplished through an original model, in which nucleation events are explicitly introduced into the Phase Field model without adding any noise term to the CH equation.

A. Critical precipitates in finite nucleation volume

By analogy with the spinodal decomposition, a non-equilibrium functional $\mathscr{V}[c]$ is calculated adding a gradient term $|\nabla c|^2$ to the non-equilibrium free energy density of the CNT $v(c)$ as discussed by many researchers[7,10,31,32]. To discuss the phase separation in *FeCr*, we model $\mathscr{V}[c]$ by a simple Landau-Ginzburg expansion:

$$\mathscr{V}[c] = \int \left[v(c) + \frac{\kappa}{2}|\nabla c|^2 - \mu(c-\bar{c}) \right] d\boldsymbol{x} \qquad (1)$$

The term μ differs from the equilibrium chemical potential and is equal to $\frac{dv}{dc}$ computed at $\bar{c}$. A sixth order Landau expansion, $v(c) = \sum_{p=0}^{3} \frac{a_{2p}}{(2p)!}(c-c_c)^{2p}$ is used to describe the iso-structural first order phase transition in *FeCr* at $7773K$

TABLE I. Landau's expansion coefficient used for computing the non-equilibrium free energy $v(c)$ and coherence length ξ associated with the Ginzburg term $\frac{\kappa}{2}|\nabla c|^2$ of $\mathscr{V}[c]$ for $FeCr$ at $773K$. The solubility limits of the equilibrium phase diagram[34] associated with $v(c)$ are also presented. For modeling the growth step, the value of the mobility, the characteristic time τ_c of the Cahn-Hilliard equation are defined. For modeling the nucleation processes, incubation times τ, cut-off concentrations c_s at which the nucleation stops, sub-volumes $\bar{V}$ as well as the nucleation time step Δt_N associated with three different metastable states of Cr composition $\bar{c}$ are also indicated. The mesh size Δx, the time step Δt and the number n^3 of sub-volumes used for the numerical resolution of the Cahn-Hilliard equation are added.

Free energy		
Landau coefficient a_0		$3.1\times10^{-1}eVnm^{-3}$
Landau coefficient a_2		$-1.67\times10^{-1}eVnm^{-3}$
Landau coefficient a_4		$-0.24\times10^{3}eVnm^{-3}$
Landau coefficient a_6		$1.96\times10^{3}eVnm^{-3}$
Solubility limits c_α, c_β		0.147, 0.853
Correlation length ξ		$3.1nm$
Micro-structure evolution		
Mobility	$M(c_\alpha)$	$1.88\times10^{-4}nm^2/seV$
Atomic volume	V_{at}	$11.82\times10^{-3}nm^3$
Scale time	$\tau_c=\frac{\xi^2}{M(c_\alpha)\lvert a_2\rvert V_{at}}$	7164 hours

Nucleation process

$\bar{c}$	Incubation time τ(h)	cut-off c_s	Sub-volume $\bar{V}$ (nm^3)	Δt_N (h)
0.19	39	0.186	9.3^3	2.5
0.198	20	0.19	6.2^3	0.05
0.206	8	0.19	5.6^3	0.06

Numerical scheme		
Mesh size Δx	$\frac{\xi}{10}$	0.31 nm
Time step Δt	$10^{-4}\tau_c$	0.02 hour
Number of sub-volumes	n^3	1000

($c_c=\frac{1}{2}$)[33]. Values of $\kappa=|a_2|\xi^2$ where ξ is the correlation length, and a_{2p} have been previously determined[14] and are summarized in table I.

The critical precipitate is the unique 1-index saddle point[35] of the functional $\mathscr{V}[c]$. It satisfies the following second-order partial differential equation[21]:

$$\frac{\partial\mathscr{V}}{\partial c(\mathbf{x})}=\kappa\Delta c-\frac{dv}{dc}-\mu=0 \tag{2}$$

For a given nucleation domain V^*, smaller than the simulation volume V, the solution of Eq.(2) exists when two boundary conditions are defined. The first boundary condition is given by $\nabla c^*(\mathbf{x})=0$ at the center of the critical precipitate. This condition avoids any cusp for $c^*(\mathbf{x})$ at $\mathbf{x}=0$. The second boundary condition results from the fact that the critical precipitate is embedded in a matrix with a Cr composition equal to c_m. This condition implies that $c^*(\mathbf{x})=c_m$ along ∂V^*.

Eq.(2) associated with such boundary conditions is a Sturm-Liouville problem and Katchaturyan[7] clearly demonstrated that $c^*(\mathbf{x})$ must be a strictly decreasing function from the center of the precipitate to the surface ∂V^*.

Unfortunately no analytical solution for Eq.(2) associated with such boundary conditions exists. Locating the saddle points in a dynamical system has been of broad interest in many fields of scientific research. One of the most important objects on the potential energy surface is the critical state, a special type of the saddle point with index 1. It is defined as a saddle point with exactly one dimensional unstable manifold. Such critical states are the bottlenecks on the most probable transition path between different local wells. For gradient flow dynamics, a large amount of numerical methods have been developed to locate these 1-index saddle points such as the climbing string method[36], the dimer method[37], or the GAD[38]. In the dimer method, the string method originally proposed for the computation of minimum energy paths is modified to find saddle points around a given minimum on a potential energy landscape using the location of this minimum as only input. The string then evolves by gradient flow in path space, with one of its end points fixed at the minimum and the other end point (the climbing image) evolving towards a saddle point according to a modified potential force in which the component of the potential force in the tangent direction of the string is reversed. The GAD approach is an improvement of the dimer method in which the Hessian is explicitly computed from the functional[39]. The exact value of the hessian then allows an accurate determination of the unique unstable manifold by a direct application of the conjugated gradient method. The main interest of the GAD method is to apply to extended systems in which the order parameter is a field. It then applies to systems associated with anisotropic electric or elastic fields.

The Gentle Ascend Dynamics (GAD) developed firstly by Rabinowitz[40] has been used for computing $c^*(\mathbf{x})$[41]. Note that such an algorithm has already been applied for computing critical precipitates for grains growth under anisotropic stress by Li[19].

From the application of the GAD, the critical precipitate $c^*(\mathbf{x})$ has been computed as a function of c_m in a given volume V^*. Figure 1 displays the composition $c^*(0)$ at the core of a critical precipitate in a finite volume V^* (red squares) as a function of c_m, the matrix Cr composition. Experimental values of $c^*(0)$ extracted from APT measurements (green dots) are in excellent agreement with values computed from the GAD assessing the validity of Eq.(2). For $\bar{c}<0.17$, $c^*(0)$ is equal to c_β as expected from the CNT. For $\bar{c}>0.17$, the composition of the critical precipitate differs from c_β expected from the CNT. Figure 1 highlights that the CNT does not predict the correct precipitate in $FeCr$ with high degree of meta-stability. The inset displays the stationary nucleation rate $J^{ss}[\bar{c}]$ and the time lag $\tau[\bar{c}]$ obtained combining the Langer's formalism and GAD approach (see[35] for details on the method). Note that $J^{ss}[\bar{c}]$ and $\tau[\bar{c}]$ exhibit non negligible values only far from the limit of validity of the CNT.

In an infinite volume V^*, c_m is equal to $\bar{c}$ as the matrix is assumed to be infinite [7]. This implies replacing a part of the matrix with $c^*(\mathbf{x})$ always satisfies the species' conservation

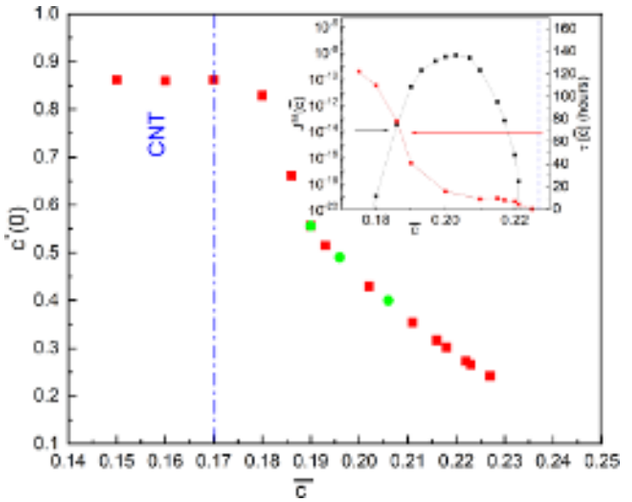

FIG. 1. Variation of $c^*(0)$ (red squares), the Cr composition at the core of a critical precipitate, computed from the GAD as a function of the Cr composition $\bar{c}$ of the metastable phase. Experimental values of $c^*(0)$ extracted from APT measurements (green dots) are also plotted. The vertical blue dashed line defines the validity range of the CNT. The inset displays the stationary nucleation rate $J^{ss}[\bar{c}]$ and the time lag $\tau[\bar{c}]$[35]

. All simulations were performed assuming $V^* = 10nm^3$ in ultra pure $Fe_{0.81}Cr_{0.19}$ samples annealed at $773K$.

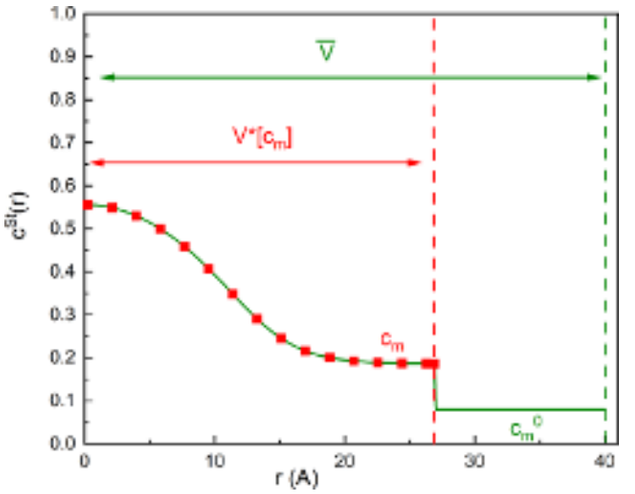

FIG. 2. Variation of profile of the stable Cr precipitate $c^{St}(r)$ as a function of the distance r from the center of the precipitate in $FeCr$ annealed at $773K$. It coincides with the profile of the critical precipitate inside V^* (red squares) and exhibits a uniform concentration $c_m^0 < c_m$ in the crown defined by $\bar{V} \setminus V^*$.

constrain. In a finite volume V^*, c_m differs from the mean Cr composition $\bar{c}$. Such a decreasing critical profile $c^*(\mathbf{x})$ never satisfies the species' conservation, *i.e.* $\frac{1}{v^*}\int_{V^*} c^*(\mathbf{x})d\mathbf{x} \neq c_m$.

Replacing part of the matrix with a critical precipitate in a finite volume V^* for modeling the nucleation process is nonphysical as it forbids the order parameter to be conservative, *i.e.* the species' conservation constrain is not satisfied.

B. Stable precipitate in finite volume

The formation of critical precipitates during the nucleation process is a spatially limited process. This implies that the order parameter is locally, *i.e.* over a characteristic length scale of few *xi*, conservative. As the critical precipitate $c^*(\mathbf{x})$ produced during the nucleation step does not satisfy the species' conservation, we introduce a mesoscopic volume $\bar{V} \supset V^*$. We then define the stable precipitate $c^{St}(\mathbf{x},t)$ as an extension of the critical profile $c^*(\mathbf{x})$ to $\bar{V}$ satisfying $\frac{1}{\bar{V}}\int c^{St}(\mathbf{x},t)d\mathbf{x} = c_m$.

From its definition, $c^{St}(\mathbf{x},t)$ can either growth or vanish in V^* as it is a critical precipitate. Replacing a part of the matrix volume by the stable precipitate insure the species' conservation, *i.e.* the order parameter is conservative as expected.

Figure 2 displays the profile of a stable precipitate in the volume $\bar{V}$. It coincides with the critical precipitate inside V^* (red squares) and exhibits a uniform concentration $c_m^0 < c_m$ in the crown defined by $\bar{V} \setminus V^*$. Along $\partial\bar{V}$, $c^{St}(\mathbf{x},t) = c_m$. Inside $\bar{V}$, the species conservation is fulfilled.

C. Determination of volumes $\bar{V}$ and V^*

To explicitly compute the stable precipitate, the volumes $\bar{V}$, V^* and the homogeneous composition c_m^0 need to be calculated as a function of c_m in the Fe-rich matrix:

$$\begin{aligned} \int_{V^*} c^{St}(\mathbf{x},t)d\mathbf{x} &= V^*\bar{c} \\ \bar{V} &= \rho(\infty)^{-1} \\ V^*\bar{c} + (\bar{V} - V^*)c_m^0(t) &= \bar{V}c_m(t) \end{aligned} \tag{3}$$

Eq.(3) highlights an implicit dependence of V^*, $\bar{V}$ and $c_m^0(t)$ with $c_m(t)$. The volume V^* is defined by the first equation in Eq.(3). It insures that the average value of the critical precipitate $c^*(\mathbf{x})$ in V^* is equal to the composition $\bar{c}$. The choice of $\bar{V}^{-1} = \rho(\infty)$ in Eq.(3) insures that the sub-volume $\bar{V}$ contains at most one stable precipitate. The term $\rho(\infty)$ is the density of precipitates at late time (cf Eq. (4)). The third equation insures that the mean composition of the stable precipitate $c^{St}(\mathbf{x},t)$ in $\bar{V}$ is always equal to $c_m(t)$.

To go a step beyond, we notice that the formation of Cr-rich precipitates induces a depletion of $c_m(t)$. This implies that $c_m(t)$ evolves with time and strictly speaking decreases from $\bar{c}$, the composition of the quenched high temperature phase to the solubility limit c_α.

The volume $\bar{V}$ can be explicitly computed from the evolution of the density of precipitates $\rho(t)$:

$$\begin{aligned} \frac{d\rho}{dt} &= J(c_m(t), \frac{t}{\tau[\bar{c}]}) \\ &= J^{ss}[c_m(t)]\, f\left(\frac{t}{\tau[\bar{c}]}\right) \end{aligned} \tag{4}$$

In Eq. (4), $J(c_m(t), \frac{t}{\tau})$ is the nucleation rate of Cr-rich precipitates embedded in a matrix of composition $c_m(t)$. The nu-

cleation rate defines the number of stable precipitates created by unit time and unit volume. It may be factorized by two distinct terms $J^{ss}[c_m(t)]$ and $f(\frac{t}{\tau[\bar{c}]})$. $J^{ss}[c_m(t)]$ is the stationary nucleation rate. It only depends on $c_m(t)$, the composition of the matrix which evolves slowly during the phase separation. Note that $c_m(0) = \bar{c}$ the Cr composition of the quenched high temperature phase. The scaling function $f(\frac{t}{\tau[\bar{c}]})$ determines the explicit time dependence of the nucleation rate. In this expression, $\tau[\bar{c}]$ is the incubation time. It only depends on the quenched high temperature phase of Cr composition $\bar{c}$. Different scaling functions $f(x)$ can be applied to model the nucleation process and they are all equivalent[42–45]. In all our simulations, $f(x)$ is assumed to be equal to $\exp(-\frac{1}{x})$ as suggested by Christian[46].

The stationary nucleation rate $J^{ss}[c_m(t)]$ and the incubation time $\tau[c]$ have been computed within the PF formalism[35]. Contrary to the CNT, this formalism insures these values are accurately calculated, whatever the degree of meta-stability $c_m(t)$ is[35].

Eq. (4) can then be solved for the initial condition $\rho(0) = 0$ under the global constrain of species conservation in the simulation volume V, *i.e.* $V\bar{c} = \int_0^t \frac{d\rho}{du}\left[\int_{V^*} c^*(\boldsymbol{x})d\boldsymbol{x}\right]du + \left[V - \int_0^t \frac{d\rho}{du}V^*du\right]c_m(t)$. This constrain leads to a set of coupled equation that dictates the evolution of $\rho(t)$ and $c_m(t)$.

Fig. 3 displays the evolution of $\rho(t)$ for different Cr composition $\bar{c}$ of the quenched high temperature phase. When $t \to \infty$, $\rho(t)$ converges to a constant value $\rho(\infty) = \bar{V}^{-1}$.

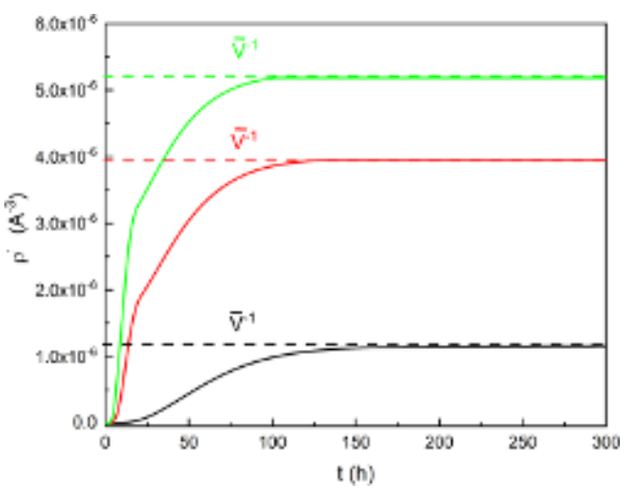

FIG. 3. Evolution of density of precipitates $\rho(t)$ calculated from Eq. (3) as a function of time for different Cr compositions of the quenched high temperature metastable phase (black line: $\bar{c} = 0.19$; red line: $\bar{c} = 0.196$; green line: $\bar{c} = 0.206$).

Strictly speaking, $c_m(t)$ decreases to c_α. As the nucleation rate J^{ss} is null at c_α, we can define a concentration threshold c_s such that $J^{ss}[c_m(t)]$ is negligible for $c_m(t) < c_s$. Note that the strong dependence of $J^{ss}[c_m(t)]$ with $c_m(t)$ implies c_s is always larger than c_α. In all our simulations, c_s is defined by $\frac{|J^{ss}[\bar{c}]-J^{ss}[c_s]|}{J^{ss}[\bar{c}]} < \varepsilon$. We checked that the tolerance $\varepsilon = 10^{-3}$ is the best trade off insuring an accurate description of the microstructure and the computational speed of the algorithm. Note that the stable profile $c^{st}(\mathbf{x},t)$ is then always chosen to have a composition equal to c_s on boundaries of the V^* domain. This composition is always lower than the Cr concentration in adjacent untransformed cells. This condition is sufficient to prevent the stable profile from becoming "subcritical" and thus shrinking during simulations.

The largest volume, V^*, is then obtained for $c_m(t) = c_s$ in Eq.(3).

Once $\bar{V}$ and V^* are computed, $c_m^0(t)$ may be calculated and the stable precipitate $c^{St}(\mathbf{x},t)$ modeling the nucleation process is then entirely determined.

The critical profile associated with the stable profile is calculated so that its composition is always equal to c_s at the boundaries of V^* and does not evolve. However, the stable profile evolves with time to ensure species conservation in $\bar{V}$ via Eq.(3). This implies that $c_m^0(t)$ evolves with time.

III. MODELING PHASE SEPARATION USING THE HYBRID METHOD

The main advantage of the CH equation is that it implicitly takes into account the growth and the coarsening of Cr-rich precipitates.

In the hybrid approach we propose, the evolution of the microstructure during the phase-separation is then dictated by the following scalar CH equation:

$$\frac{\partial c(\boldsymbol{x},t)}{\partial t} = \nabla.\left[M(c(\boldsymbol{x},t))\nabla\frac{\partial \mathscr{V}[c]}{\partial c(\boldsymbol{x},t)}\right] \tag{5}$$

where $M(c)$ is the concentration-dependent mobility. It is assumed to be constant in the following (cf table I).

To solve Eq. (5), boundary conditions must be specified. We assume that $\nabla c = 0$ and $\nabla\frac{\partial \mathscr{V}[c]}{\partial c} = 0$ at the boundary ∂V of the simulation volume V. To avoid any edge effects, the Cr composition $c(\mathbf{x},t)$ defining the microstructure is assumed periodic.

Unfortunately, the non-linear part of $\mathscr{V}[c]$ prohibits any analytical solution for Eq. (5). Based on Eyre's procedure[47], we have developed a numerical scheme to solve the CH equation in Fourier space[48]. This gradient stable scheme ensures an efficient trade-off between computational speed and the accuracy of the numerical solution[48].

In our hybrid method, no noise has been added to Eq. (5) for modeling the nucleation step. We model the homogeneous nucleation process injecting stable precipitates $c^{St}(\mathbf{x},t)$ in V at different times. The injection rate of these stables precipitates is dictated by the nucleation rate.

Such an approach then allows modeling the interplay between the nucleation, the growth and the coarsening steps without evoking any characteristic time scale. As the computation of the stable precipitate, the nucleation rate and the incubation time are derived from the PF formalism, the method we propose applies whatever the degree of meta-stability is. It then allows a direct comparison with experiments.

Some authors[19,49,50] have previously propose such an hybrid method for modeling the phase separation in the nucleation and growth regime. However, physically sounded bases for stable precipitates is not discussed by these authors and nucleation rates are always computed within the CNT forbidding any comparison with experimental measurements.

A. Injection rate of stable precipitates: a Monte-Carlo approach

The nucleation step during the simulation is modeled by injecting in the simulation volume V, stable precipitates into n^3 mesoscopic sub-volumes labeled $\bar{V}_r$. Each sub-volume $\bar{V}_r$ contains either one or zero stable precipitate (cf Fig. 4).

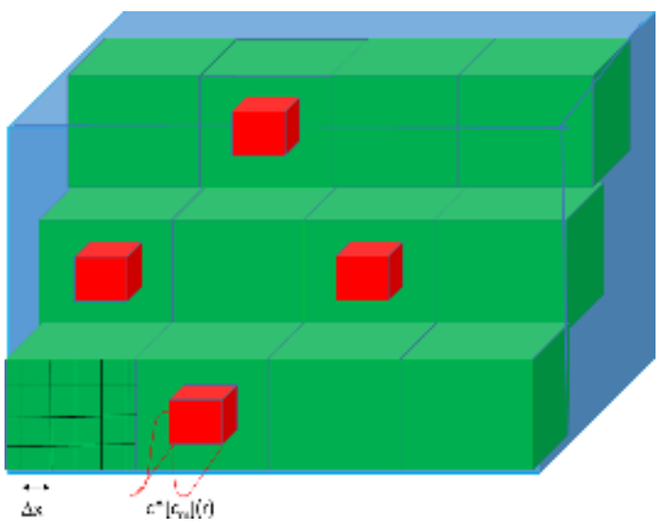

FIG. 4. Schematic description of the simulation volume V (blue cube). This volume is split into n^3 sub-volumes $\bar{V}_r$ (green cubes). In each of these sub-volumes, the average Cr concentration is equal to c_m. Inside each sub-volume $\bar{V}_r$, zero or one stable precipitate (red line) can be injected via a Monte-Carlo procedure at each nucleation time. This profile is critical in the volume V^* (red cubes). On this graph, the spatial mesh Δx (black grid) used in the numerical resolution of the CH equation is also plotted.

As the nucleation process is a rare event, it can then be modeled by a Poisson process of parameter $\lambda_r(t) = J^{ss}[c_r(t)]exp(-\tau[\bar{c}]/t)\bar{V}\Delta t_N$. The time step Δt_N is the duration between two injections. It is selected imposing that the maximum number of injected stable profiles in the volume V is smaller than $\frac{n^3}{10}$, *i.e.* $\Delta t_N = \frac{1}{10\bar{V}J^{ss}[\bar{c}]}$. The injection rate $\frac{d\langle N(t)\rangle}{dt}$ where $\langle N(t)\rangle$ is the mean number of stable precipitates at time t reduces to $\frac{d\lambda_r(t)}{dt}$. As $\lambda_r(t)$ only depends on the sub-volume $\bar{V}_r$, the injection rate is local as expected for a nucleation process.

Fig. 5 displays the fraction of stable precipitates (black squares) and the cumulative fraction of stable precipitates injected during the simulation (red line) in $Fe_{0.81}Cr_{0.19}$ samples annealed at $773K$.

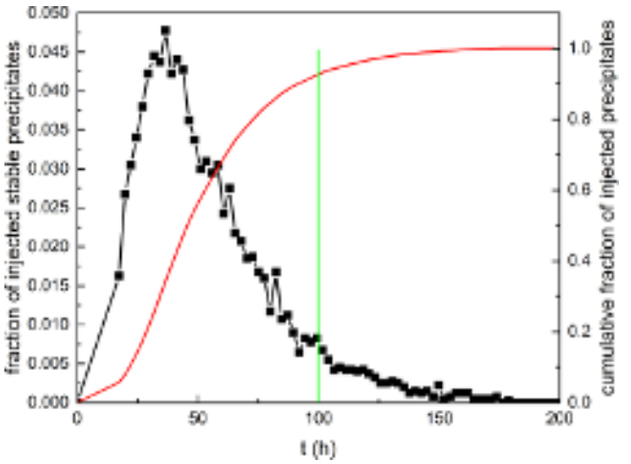

FIG. 5. Fraction of stable precipitates (black squares) injected into the simulation volume V by the MC algorithm as a function of time in $Fe_{0.81}Cr_{0.19}$ annealed at $773K$. The delay between two injections (black square) is constant and equal to Δt_N . The red curve shows the cumulative fraction of stable precipitates injected. For comparison, the green vertical curve shows the total fraction (95%) of injected stable profiles at 100 hours[14].

Inspection of Fig. 5 highlights that 95% of stable profiles are injected before 100 hours (vertical green line). This justifies the PF calculations previously performed[14]. These calculations assumed that all stable precipitates are produced at 100 hours and define the initial condition of the CH equation[14].

B. Description of the algorithm

The hybrid algorithm used to model the phase separation is described in detail in the flowchart shown in Fig 6. It differs from previously proposed algorithms[49–51]:

- The method we propose is conservative. The stable precipitate $c^{St}(\boldsymbol{x},t)$ modeling the nucleation process then satisfies the species conservation in each volume $\bar{V}_r$ as expected.
- The nucleation rate $J_r(t)$ is local, *i.e.* it is defined over the volume $\bar{V}_r$. It is obtained from the sole knowledge of the non-equilibrium free energy functional $\mathscr{V}[c]$. Moreover, it then does not suffer from the CNT limitation, allowing direct comparison with experimental results.
- No characteristic time scale is introduced to distinguish nucleation, growth and coarsening processes.

IV. COMPARISON BETWEEN SIMULATED AND EXPERIMENTAL MICROSTRUCTURES

To validate our hybrid method, not only the density but also the characteristic size and the compositions of Cr-rich precipitates (Fe-rich matrix respectively) resulting from 3D simu-

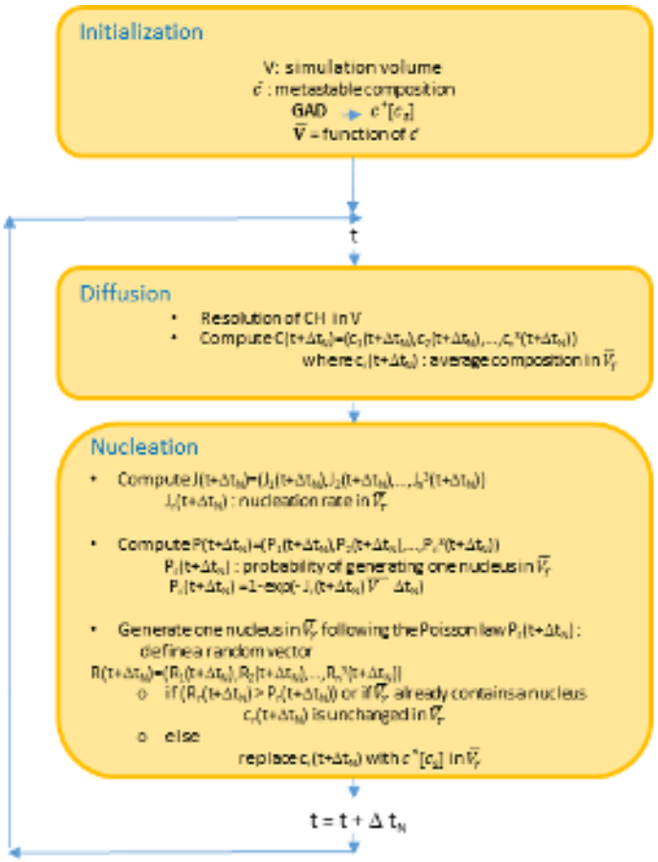

FIG. 6. Flow chart of the hybrid model used for mimicking the nucleation and growth process. For all sub-volumes, the average $C(t)$ composition vector, the nucleation rate $J(t)$ vector and the probability $P(t)$ of replacing a sub-volume with a stable precipitate are computed at each nucleation time step. A Monte-Carlo procedure is then applied for selecting random sub-volumes and the CH equation is numerically solved between two nucleation time steps. This procedure is applied until the final time.

lations have been directly compared with measurements extracted from APT measurements[26–28].

A. Phase separation in $Fe_{0.81}Cr_{0.19}$ samples annealed at $773K$

To highlight the advantages of our hybrid method, we also compared our 3D simulations with previous simulations[27]. These previous simulations have been performed assuming that the 3D microstructure generated at the end of the nucleation process is the initial for the CH equation, *i.e.* the nucleation and growth process act sequentially during the phase separation. In such an approach, solving the CH equation required knowing the density of the stable profiles, when injected.

Our approach bypasses this limitation, enabling the microstructure to be calculated solely on the basis of the $\bar{c}$ composition of the metastable state. This is the key point of our hybrid method. All parameters for 3D simulations of the microstructure performed using either the hybrid method or the previous approach[14] are summarized in table I and no parameters have been fitted.

To allow a direct comparison between simulations and APT measurements, we define Cr-rich precipitates in our 3D simulations in a similar way to those resulting from the analysis of APT measurements. A precipitate is assumed to be created as soon as the local concentration $c(\boldsymbol{x},t)$ exceeds a given concentration threshold $c_t = 0.28$[27]. The radius R of the precipitate is then defined by $c(R,t) = c_t$ for both APT measurements and numerical simulations.

To demonstrate that our hybrid approach reproduces well the morphology of the microstructure, i.e. the spatial distribution of precipitates, we have plotted on Figure 7 the comparison between microstructures measured by APT and simulated by the hybrid method. Note that the ellipsoidal shape of Cr-rich precipitates at long times is an artifact of the APT method. This is due to a local magnification effect caused by the difference in evaporation fields between the Cr-rich and Cr-poor phases[52,53]. In reality, Cr-rich precipitates are spherical, in agreement with PF simulations[52,53].

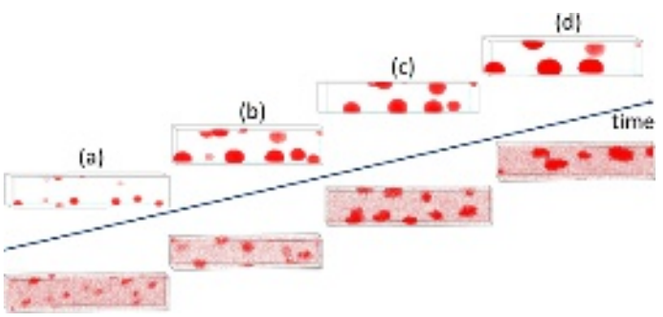

FIG. 7. Comparison between the simulated (top graphs) and measured (bottom graphs) snapshots of the microstructure at different times (a: 100 hours; b:500 hours; c:1000 hours and d:2000 hours).

Fig 8 displays the evolution of the density $\rho(t)$ (black line on graph a) and mean radius $\langle R(t)\rangle$ (black line graph b) of *Cr*-rich precipitates extracted from 3D simulations computed using our hybrid formalism.

These simulations are in excellent agreement with results of APT measurements (red squares). As shown in Fig 8, the density $\rho(t)$ of Cr-rich precipitates derived from our modeling for $t < 170$ hours is in excellent agreement with experimental measurements[27] in contrast to the simulations carried out previously (green curve in Fig 8). These results justifies the validity of our hybrid method for modeling the nucleation process. Note that the mean size and the composition of Cr-rich precipitates experimentally observed for $t < 100$ hours are identical to the calculated stable precipitates computed from Eq.(2).

The evolution of the density $\rho(t)$ and mean radius $\langle R(t)\rangle$ of Cr-rich precipitates allow defining three different steps, as expected. In the nucleation step (N), *i.e.* for $t < 170$ hours, the mean radius is constant with time. In the growth step (G), *i.e.* for $170 < t < 400$ hours, the mean radius follows a square-root law. In the coarsening regime (C) , for $t > 400$ hours,

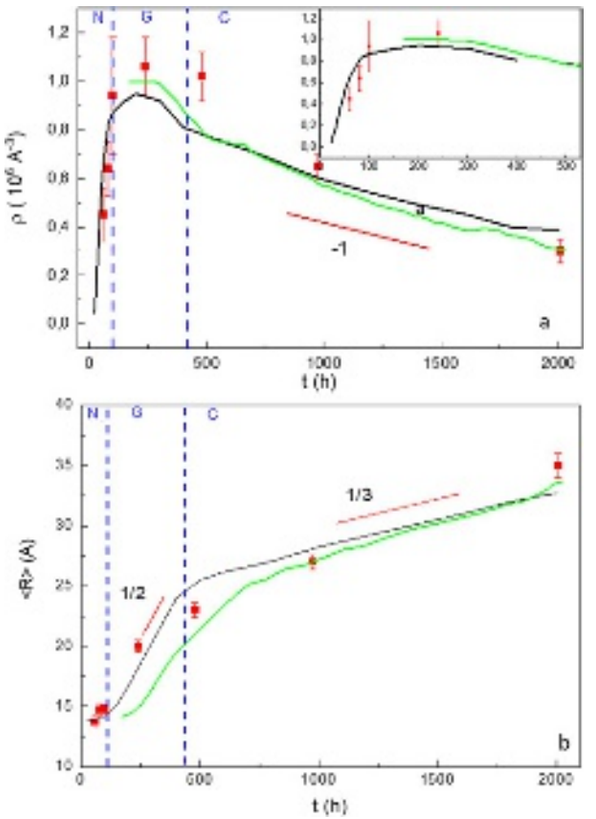

FIG. 8. Comparison between the density $\rho(t)$ and the mean radius $\langle R(t)\rangle$ as a function of time (black line: our simulation of the nucleation and growth process; green line: solution of the CH equation with initial conditions dictated by experimental measurements at 170 hours[14]; red squares: extracted from APT measurement on ultra-pure $Fe_{0.81}Cr_{0.19}$ samples annealed at $773K$. Limits of the nucleation N, the growth G and the coarsening regime C are plotted as vertical dashed blues lines.

$\langle R(t)\rangle \approx t^{\frac{1}{3}}$ and $\rho(t) \approx t^{-1}$ as predicted by the LSW approach during the coarsening step.

As expected from inspection of Fig. 5, previous simulations (green line on the inset of graph a on Fig 8) are enable to model the nucleation process which mainly occurs below 170 hours. However, the growth and coarsening steps are reproduced by our previous modeling. This good agreement observed after 170 hours is due to the small value of the mobility at this temperature leading to a very small growth of stable precipitates. Note that the hybrid method better describes the time evolution of the mean radius $\langle R(t)\rangle$ of Cr-rich precipitates at late time than the previous simulations. This point highlights the necessitate to accurately model the nucleation step. The late time microstructure depends on this modeling.

The evolution of the composition of Cr-rich precipitates and the Fe-rich matrix has also been compared with experimental results and previous simulations. Such an evolution is displayed on Fig 9. The top graph on Fig 9 validates that our hybrid model is conservative. The Cr composition averaged over the simulation volume V, $\langle c\rangle$, remains always close to $\bar{c}$ as expected.

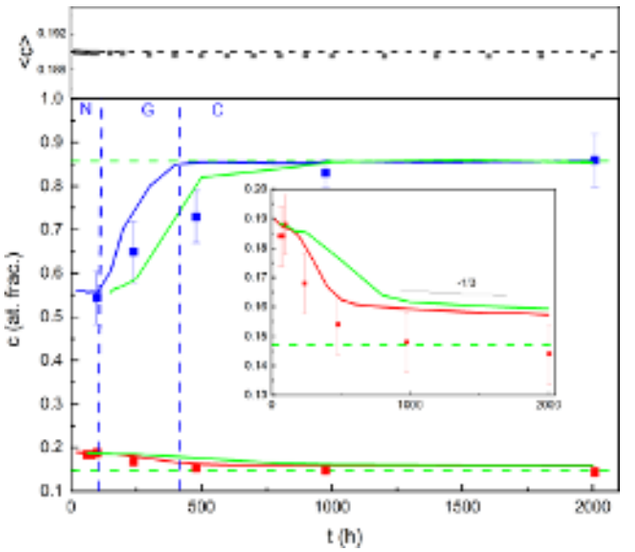

FIG. 9. Evolution of Cr-concentration at the core of Cr-rich precipitates (blue) and in the matrix (red) as a function of time (square: APT measurements; lines: simulations resulting from the hybrid model) and compared with previous simulations (green lines). The solubility limits of the equilibrium phase diagram at $773K$ are plotted as horizontal green dashed lines. The zoom of the matrix composition is plotted in the inset. The top graph displays the evolution of the average concentration $\langle c(t)\rangle$ in the simulation volume V (black squares) and $\bar{c}$ is displayed as a black dashed line.

Note that graph b on Fig 8 is shifted from 70 hours in comparison with previous published results (Fig.7 in[14]). Experimental data plotted on graph a on Fig 8 allows to accurately measure the duration of the nucleation process. it is equal to 170 hours and differs from the previous value of 100 hours (vertical green line on Fig 5).

These results highlight the quality of our hybrid model. It is able to reproduce the increasing of the Cr composition in the growth step, never modeled by Atomic Kinetic Monte-Carlo or previous PF simulations[54,55].

Despite the composition of the Fe-rich matrix extracted from the hybrid models (red line) better reproduces the experimental evolution of $c_m(t)$ than the previous model, this is not the case for the composition of Cr-rich precipitates. The reason is yet unknown. Note that the inset in Fig. 9 shows a systematic overestimation of the Cr composition of the matrix experimentally observed. This overestimation may be due to the erroneous value of the solubility limit $c_\alpha = 0.147$ extracted from Calphad[34]. Our simulations confirm Novy's[26] observations and clearly show that this overestimation should disappear for a choice of the solubility limit c_α equal to 0.14.

B. Main interest of the hybrid approach

The main advantage of the hybrid method we present is that phase separation can be modeled using only the aver-

age composition $\bar{c}$ of the quenched high-temperature phase and the non-equilibrium free energy functional $\mathscr{V}[c]$. To validate this point, the hybrid approach has been applied to model the phase separation in the *FeCr* alloys with mean Cr compositions equal to 0.198 and 0.206 and compare with APT measurements[26,28]. In contrast to the previous case, no measurement of the nucleation step is available and the phase-separation must be modeled from scratch using the hybrid approach.

All 3D simulations were performed using parameters summarized on table I. No adjustments were applied. The threshold values for defining the Cr-rich precipitates have been fixed to 0.35[28] and 0.4[26] insuring a direct comparison of simulations with APT measurements.

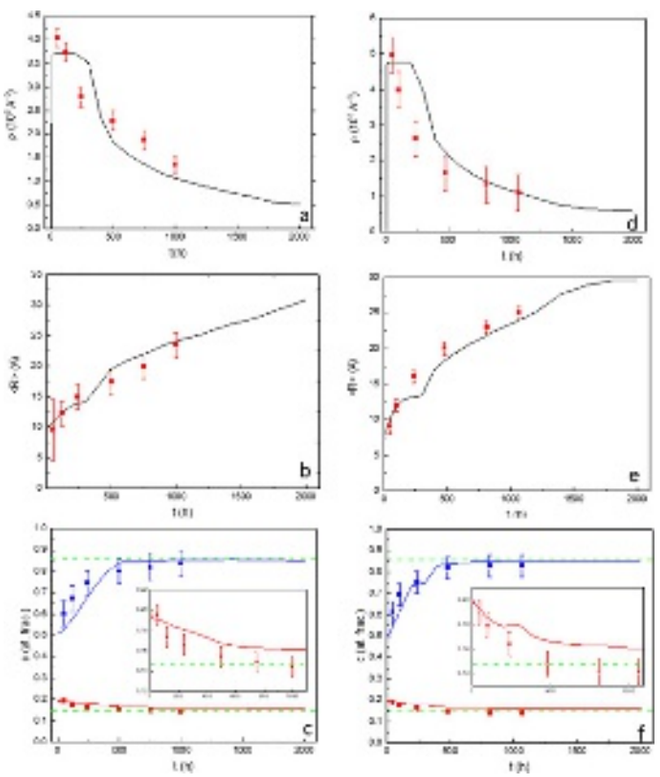

FIG. 10. Comparison between the experimental (squares) and simulated (full line) densities $\rho(t)$ and mean radii $\langle R(t)\rangle$ of Cr-rich precipitates as a function of time. Concentration at core of Cr-rich precipitates (blue) and in the Cr-poor matrix (red) are also plotted. The solubility limits derived from Calphad[34] are also plotted (green dashed line). Note that $\bar{c} = 0.198$ for graphs a,b and c and $\bar{c} = 0.206$ for graphs d,e and f.

The evolution of the simulated densities $\rho(t)$, mean radii $\langle R(t)\rangle$ and core compositions $c_p(0)$ of *Cr*-rich precipitates as well as the composition of the *Fe*-rich matrix $c_m(t)$ are plotted on Fig 10. Comparison with experimental measurements performed at late time are in excellent agreement validating the hybrid method.

V. VALIDITY OF THE JMAK THEORY FOR DIFFUSIVE SYSTEMS

The theory of overall kinetics of phase transformation involving nucleation and growth process is due to Johnson[15], Mehl[16], Avrami[17] and Kolmogorov[18] and is now known as the JMAK theory. This approach models for instance the evolution of the volume fraction $f_V(t)$ of the new phase during the grains growth.

The JMAK theory is based on several assumptions: critical precipitates randomly nucleate in an infinite matrix, they grow isotropically at a constant rate and they stop to grow at any point the precipitate impinges other precipitates. This is known as the hard impingement model.

Despite the mathematical derivation of the JMAK is complicated[18], the final expression simply writes[18]:

$$f_V(t) = 1 - exp(-f_V^{ex}(t)) \tag{6}$$

where $f_V^{ex}(t)$ is the extended volume fraction of the new phase resulting from the nucleation and growth process of an "effective " precipitate without impingement in an infinite matrix[45].

The key point of this analysis is that $f_V^{ex}(t)$ is a simple convolution of the nucleation rate $J(t)$ and the volume of the precipitate $V(t)$, *i.e.* $f_V^{ex}(t) = \int_0^t J(u)V(t-u)du$.

The main ingredient of the JMAK theory is to assume that $f_V^{ex}(t)$ writes kt^n. In this expression, n is the Avrami exponent independent of the temperature T. The Avrami exponent n is a constant which only depends on the shape and the spatial distribution of precipitates[56,57]. The term $k(T) = k_0 exp(-\frac{E_a}{k_B T})$ follows an Arrhenius dependence with the temperature[16]. The terms k_0 and E_a are the reaction rate and the activation energy respectively. This formulation allows defining the so called Time-Temperature Transformation curves (TTT) , extensively used in metallurgy to discuss the materials properties[45].

A. Soft impingement and diffusive systems

In diffusive systems, the growth of precipitates depletes the matrix via a long range diffusion field[58]. In these systems, the growth of precipitates is limited by the interaction between these diffusion fields leading to the notion of soft-impingement.

Despite the existence of such a long range field, extension of the JMAK theory to diffusive first-order phase transitions assumes that the notion of extended volume still holds. Since the volume fraction of precipitates is only a fraction of the volume V, Eq. (6) is then replaced by:

$$\frac{f_V(t)}{f_V(\infty)} = 1 - exp(-kt^n) \tag{7}$$

where $f_V(\infty)$ is the equilibrium volume fraction measured at late time.

The existence of long range diffusion fields lead some doubts on the application of the JMAK theory to diffusive

first-order phase transitions. In particular, the Avrami exponent n is no more constant as it is the case for hard impingement and seems to vary with time. On the experimental side, the validation of the JMAK theory is polluted by spurious effects like transients, non spherical growth, multiple face formation and heterogeneous nucleation. Simulations of the nucleation and growth process presented in this work may then be an efficient alternative to check the validity of the JMAK theory for diffusive first-order phase transitions.

Incorporating explicitly the nucleation algorithm, our hybrid methods derived from the PF approach can evaluate self-consistently the long range diffusive field during the growth and coarsening process. these ability considerably relief the restrictions imposed by analytical models dealing with the soft impingement[56,57,59].

B. The hybrid model and the JMAK theory

Fig 11 displays the evolution of the volume fraction of *Cr*-rich precipitates $f_V(t)$ as function of time extracted from our simulations for $\bar{c}$ equal to 0.19, 0.198 and 0.206 respectively. For all curves, $f_V(t)$ is null at short time and tends to the equilibrium volume fraction $f_V(\infty) = \frac{(\bar{c}-c_\alpha)}{(c_\beta-c_\alpha)}$ at large time.

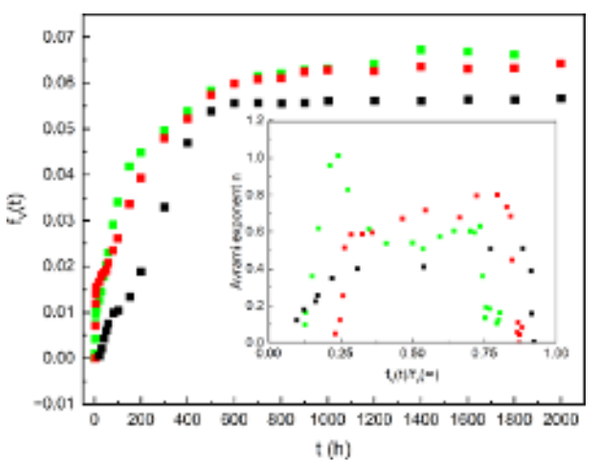

FIG. 11. Evolution of the volume fraction $f_V(t)$ extracted from our 3D simulations versus time. As expected, the volume fractions increase and tend to their equilibrium values $f_V(\infty)$ at large time (black squares: $\bar{c} = 0.190$; red squares: $\bar{c} = 0.198$; green squares: $\bar{c} = 0.206$). The inset displays the evolution of the Avrami exponent n as a function of the dimensionless volume fraction $\frac{f_V(t)}{f_V(\infty)}$.

From Eq.(7), the evolution of the Avrami exponent is given by:

$$n = \frac{dln(ln(1-\frac{f_V(t)}{f_V(\infty)}))}{dln(t)} \tag{8}$$

This exponent is plotted on the inset of Fig 9 as a function of the dimensionless volume fraction $\frac{f_V(t)}{f_V(\infty)}$. For the diffusive phase separation, the Avrami exponent n is no more constant. Asymptotic values of n for $\frac{f_V(t)}{f_V(\infty)} \to 0$ and $\frac{f_V(t)}{f_V(\infty)} \to 1$, *i.e.* a short and large time, can be understood:

- At short time, *i.e.* in the nucleation step, $\frac{f_V(t)}{f_V(\infty)} \approx 0$ and $R(t)$ remains constant as displayed on Fig 9 and Fig 10. The time integration of $f_V^{ex}(t)$ can then be analytically computed and reduces to $J^{ss}[\bar{c}]\Gamma(-1, \frac{\tau[\bar{c}]}{t})$ where Γ is the incomplete gamma function. As $\Gamma(-1, \frac{\tau[\bar{c}]}{t})$ tends to 0 at short time, the Avrami exponent must then be null for $\frac{f_V(t)}{f_V(\infty)} \to 0$. This analysis agrees with numerical results plotted on the inset of Fig 11.

- At large time, *i.e.* in the coarsening step, the dimensionless volume fraction tends to 1 and the microstructure results from *Cr*-rich precipitates of radius $R(t)$ embedded in a *Fe*-rich matrix. The Gibbs-Thomson effect[60] implies that the composition of precipitates, $c_p(R(t)) = c_\beta + \frac{2\sigma}{R(t)(c_\beta-c_\alpha)\frac{d^2v}{dc^2}(c_\beta)}$ is constant inside each precipitate and only depends on its radius $R(t)$. In this expression, σ is the interfacial free energy and only depends on ξ and the non-equilibrium free energy density $v[c]$[7,14]. In the nucleation and growth regime, $\frac{d^2v}{dc^2}(c_\beta) > 0$. Performing a first order expansion of $f_V(t) = \frac{[\bar{c}-c_m(t)]}{[c_p(R(t))-c_m(t)]}$ with respect to $R(t)^{-1}$ with $c_m(t) \approx c_\alpha$, $f_V(t)$ writes $1 - \frac{A}{R}$ where $A = \frac{2\sigma}{(c_\beta-c_\alpha)^2\frac{d^2v}{dc^2}(c_\beta)}$ is always positive. As $R(t)$ follows the LSW scaling law at large time, $n \approx ln(t)^{-1}$ and then vanishes when $\frac{f_V(t)}{f_V(\infty)} \to 1$ in agreement with numerical results displayed on the inset of Fig 9.

The hybrid method we propose makes it possible to discuss the relevance of the proposed JMAK theory for describing conservative diffusive phase separation. Calculation of the Avrami exponent for 3D simulations shows that the existence of a long-range diffusion field precludes the use of the JMAK approach for conservative systems. Only a complete modeling of phase separation can correctly describe the evolution of the microstructure. Note that for the non conservative Allen-Cahn dynamics, there is no conservative "concentration field" and the JMAK applies[61].

VI. CONCLUSION

The kinetic of phase separation in *FeCr* alloys, a textbook example of diffusive first order phase transition, has been modeled in detail using an hybrid phase field method.

As already proposed by some authors[49,50], the hybrid method consists in simulating homogeneous nucleation by injecting stable precipitates randomly into a simulation volume and modeling their evolution by the Cahn-Hilliard equation. The excellent agreement between simulations and experimental measurements performed in *FeCr* samples of different compositions validates our model.

This work demonstrates that the hybrid method is able to compute the microstructure induced by phase separation during thermal annealing from the sole knowledge of the composition of the initial quenched high temperature phase and the non-equilibrium free energy functional $\mathscr{V}$.

Application of our model highlights that the soft impingement model based on the JMAK theory cannot model the evolution of the microstructure in diffusive phase separation. This work explains physical reasons associated with the failure of the JMAK approach. It results from the existence of a long range diffusive fields imposed by the species' conservation constrain in conservative systems.

This method is quite general and can be straightforwardly applied to more complex phase separations including not only conservative but also non conservative order parameters that control phase separation in oxides or precipitation in multi-components alloys. By its ability to compute order parameters fields, the hybrid method can been applied to model phase-separations under non isothermal conditions, *i.e.* microstructures of industrial materials resulting of complex thermal histories.

[1] D. Oxtoby, J. Phys.: condens. Matter **4**, 7627 (1992).
[2] L. Grasnasy and P. James, J. of non Cryst. Solids **253**, 210 (1999).
[3] C. Nanev, Progress in Crystal Growth and Characterization of Materials **66**, 100484 (2020).
[4] N. E. Chayen, Progress in Biophysics and Molecular Biology **88**, 329 (2005).
[5] S. Puri and V. Wadhawan, *Kinetics of phase transitions* (Taylor and Francis Group, LLC, 2009).
[6] K. Binder and P. Fatzl, *Phase transformation in Materials: Spinodal decomposition* (Wileu-VCH, 2001).
[7] A. G. Katchaturyan, *Theory of structural transformation in solids* (Wiley Interscience, 1983).
[8] P. E. L'vov and V. V. Svetukhin, Phys. Solid State **57**, 1213 (2015).
[9] A. Bray and K. Humayn, Phys. Rev. Lett. **68**, 1559 (1992).
[10] J. Langer, Annals of Physics **65** (1971).
[11] D. Gunton, M. San Migel, and P. Sahni, Phase transition and Critical Phenomena **8**, 1755 (1983).
[12] P. G. Debenedetti, Y.-Y. Kim, F. C. Meldrum, and H. Tanaka, The Journal of Chemical Physics **160**, 100401 (2024), https://pubs.aip.org/aip/jcp/article-pdf/doi/10.1063/5.0203119/19720601/100401_1_5.0203119.pdf.
[13] A. Aasen, Wilhelmsen, M. Hammer, and D. Reguera, The Journal of Chemical Physics **158**, 114108 (2023), https://pubs.aip.org/aip/jcp/article-pdf/doi/10.1063/5.0142533/18009695/114108_1_5.0142533.pdf.
[14] O. Tissot, P. Gokelaere, P. Garcia, L. Pauchard, C. Pareige, L. Luneville, and D. Simeone, Acta Materialia **260**, 119303 (2023).
[15] W. A. Johnson and R. F. Mehl, Transactions of the American Institute of Mining and Metallurgical Engineers **135**, 416 (1939).
[16] R. F. Mehl and R. W. Cahn, *Physical Metallurgy, vol 1* (R. W. Cahn and P. Haasen, North-Holland Physics Publishing, 1983).
[17] M. Avrami, The Journal of Chemical Physics **7**, 1103 (1939).
[18] K. A., Izv Akad Nauk SSSR **3**, 355 (1937).
[19] Y. Li, S. Hu, L. Zhang, and X. Sun, Modelling and Simulation in Materials Science and Engineering **22**, 025005 (2014).
[20] J. W. Cahn and J. E. Hilliard, J. of Chem. Phys. **28**, 258 (1958).
[21] J. W. Cahn and J. E. Hilliard, J. of Chem. Phys. **31**, 688 (1959).
[22] J. W. Cahn, J. of Chem. Phys. **30**, 1121 (1959).
[23] R. Becker and W. Doring, Ann. Phys. **416**, 719 (1935).
[24] J. Zeldovich, Acta Phys. Chem. USSR **18**, 7 (1943).
[25] M. Volmer and A. Weber, Zeitschrift für physikalische Chemie **1**, 119 (19262).
[26] S. Novy, P. Pareige, and C. Pareige, J. of Nucl. Mater. **384**, 96 (2009).
[27] O. Tissot, *Effet de l'irradiation sur la démixion du Cr dans les alliages Fe-Cr*, Ph.D. thesis, Université de Rouen - Normandie (2016).
[28] S. K. Sarkar, D. Ray, D. Sen, and A. Biswas, Microscopy and Microanalysis **29**, 437 (2023).
[29] A. Ardell, Acta Metallurgica **20**, 61 (1972).
[30] H. E. Cook, Acta Metallurgica **18**, 297 (1970).
[31] J. W. Cahn, Acta Metall. **9**, 795 (1961).
[32] K. Binder and D. Stauffer, Advances in Physics **25**, 343 (1976).
[33] J. Tolédano and P. Tolédano, *The Landau Theory Of Phase Transitions: Application To Structural, Incommensurate, Magnetic And Liquid Crystal Systems* (World Scientific Lecture Notes in Physics, 1986).
[34] A. Jacob, E. Povoden-Karadenzi, and E. Kozeschnik, Calphad **60**, 16 (2018).
[35] D. Simeone, P. Garcia, O. Tissot, and L. Luneville, Phys Rev Lett. **131**, 117101 (2023).
[36] T. Philippe and D. Blavette, Journal of Chemical Physics **135**, 134508 (2011).
[37] G. Henkelman and H. J´onsson, J. Chem. Phys. **111**, 7010–7022 (1999).
[38] L. Zhang, L.-Q. Chen, and Q. Du, Phys. Rev. Lett. **98**, 265703 (2007).
[39] A. Heyden, A. Bell, and F. Keil, J. Chem. Phys. **123**, 224101 (2005).
[40] P. Rabinowitz, *Methods in critical point theory with application to differential equations* (American Mathematical Society, 1986).
[41] L. Luneville, P. Garcia, O. Tissot, and D. Simeone, Appl. Phys. Lett. **121**, 184102 (2022).
[42] K. Trinkaus, Phys Rev B **27(12)**, 7372 (1983).
[43] D. Kashchiev, *Nucleation: Basic Theory with Applications* (Oxford, 2000).
[44] A.Kantrowitz, J. Chem. Phys. **19**, 1097 (1951).
[45] P. Papon, J. Lebloc, and P. Meijer, *Physics of phase transition* (Dunod, 1999).
[46] J. Christian, *The Theory of Transformations in Metals and Alloys* (Pergamon Press, Oxford, 1975).
[47] D. J. Eyre, MRS Proceedings **529**, 39 (1998).
[48] D. Simeone, P. Garcia, and L. Luneville, Materials **15(9)**, 2991 (2022).
[49] J. Simmons, C. Shen, and Y. Wang, Scripta mater. **43**, 935–942 (2000).
[50] J. Simmons, Y. Wen, C. Shen, and Y. Wang, Materials Science and Engineering **A365**, 136–143 (2004).
[51] A. Jokisaari, C. Permann, and K. Thornton, Computational Materials Science **112**, 128 (2016).
[52] F. Vurpillot, A. Bostel, and D. Blavette, Applied Physics Letters **76**, 3127 (2000).
[53] C. Hatzoglou, B. Radiguet, G. Da Costa, P. Pareige, M. Roussel, M. Hernandez-Mayoral, and C. Pareige, Journal of Nuclear Materials **522**, 64 (2019).
[54] E. Martinez, O. Senninger, C. Fu, and F. Soisson, Phys. Rev. B **86**, 224109 (2012).
[55] T. Barkar, L. Hoglund, J. Odqvist, and J. Agren, Computational Materials Science **143**, 446 (2018).
[56] D. Crespo, T. Pradell, M. T. Clavaguera-Mora, and N. Clavaguera, Phys. Rev. B **55**, 3435 (1997).
[57] F. Ham, The Journal of physics and chemistry of solids **6**, 335 (1958).
[58] J. Marqusee and J. Ross, J. of Chem. Phys. **80**, 5361 (1984).
[59] T. Pradell, D. Crespo, N. Clavaguera, and M. T. Clavaguera-Mora, Journal of Physics: Condensed Matter **10**, 3833 (1998).
[60] D. Simeone, P. Garcia, O. Tissot, and L. Luneville, J. of Appl. Phys. **131**, 165110 (2022).
[61] M. Iwamatsu, The Journal of Chemical Physics **128**, 1.2883652 (2008).